

Gradient-boosted equivalent sources

Santiago R. Soler^{1,2}  and Leonardo Uieda³ 

¹Consejo Nacional de Investigaciones Científicas y Técnicas (CONICET), Ciudad Autónoma de Buenos Aires, Argentina

²Instituto Geofísico Sismológico Volponi, Universidad Nacional de San Juan, San Juan, Argentina

³Department of Earth, Ocean and Ecological Sciences, School of Environmental Sciences, University of Liverpool, UK
santiago.r.soler@gmail.com

2021

Accepted 2021 July 27. Received in original form 2021 February 21.

Disclaimer: This is a pre-copyedited, author-produced PDF of an article published in *Geophysical Journal International* following peer review. It is available from EarthArXiv at doi.org/10.31223/X58G7C. The version of record “Soler & Uieda (2021). Gradient-boosted equivalent sources. *Geophysical Journal International*. doi:10.1093/gji/ggab297” is available online at doi.org/10.1093/gji/ggab297.

License: © 2021 Santiago R. Soler and Leonardo Uieda. Available under a Creative Commons Attribution 4.0 International license ([CC-BY](https://creativecommons.org/licenses/by/4.0/)).

Abstract

Paleomagnetism is the main tool used in paleogeographic reconstructions, in which directional information of the past magnetic field is retrieved from ferromagnetic grains (l.s). Magnetic minerals have a wide range of size and composition that influence their magnetic properties and, consequently, their ability to record the directions of paleomagnetic fields. The signals obtained with classical paleomagnetic methodologies are vector averages that include all magnetic grains present in the samples, including the stable and unstable carriers. To improve the quality of the magnetic signal, it would be necessary to individually identify the magnetizations of the carriers of remanent magnetization, in order to isolate only the good registers of the geomagnetic field. This would allow obtaining more reliable paleomagnetic information, as well as possibly being effective for the paleomagnetic study of older rocks (e.g., Archean rocks), meteorites and even bodies with complex geological evolution. Therefore, this project aims to apply magnetic microscopy to identify the remanent magnetization directions of stable magnetic grains and, subsequently, invert these data in an attempt to recover the individual paleomagnetic directions of the magnetic carriers present in the thin-sections. If successful, a new precision methodology for paleomagnetic data acquisition will be implemented.

Keywords: Paleomagnetism, magnetic microscopy, Euler deconvolution, inversion of magnetic data.

1 Introduction

Paleomagnetism is the study of the record of the Earth’s magnetic field preserved in rocks, being the main tool, and the only quantitative method, used during paleogeographic reconstruction (?). It is based on three basic assumptions: (i) the geomagnetic field can be approximated to the field created by a geocentric axial dipole (GAD) aligned with the Earth’s axis of rotation over a period that eliminates paleosecular variation ($> 10^4$ years) (?); (ii) ferromagnetic minerals (l.s.) acquire natural remanent magnetization (NRM) parallel to the Earth’s geomagnetic field (??); and (iii) this acquired magnetization is recorded for a long period of time, depending on the physicochemical characteristics of the magnetized mineral, following Neél’s Theory (??) and being also influenced by the geological processes by which the rocks were submitted.

The thermoremanent magnetizations (TRMs) of magnetic particles in geological materials are the main records of the direction of the geomagnetic field of the past (?). Iron oxides, such as magnetite, which is the most common magnetic mineral present in rocks (?) and acquire TRM as they cool below their Curie temperature and subsequently this direction of magnetization is “frozen” upon reaching blocking temperature (?).

When the grains are small enough, and the magnetization is unidirectional homogeneous (single domain - SD), the acquisition and preservation of magnetic signals is physically supported by Néel's theory (??), conserving the remanent magnetization for long periods of time, on the order of billions of years, and for this reason, they are considered “good recorders” of the paleomagnetic field. In addition to SD, pseudo-single domain (PSD) particles, in the flower and stable vortex states, can also preserve magnetization for periods on the order of the solar system age (?). On the other hand, Néel's theory does not cover larger particles (multi domain - MD), which have unstable remanent magnetization (e.g., caused by viscous reordering of magnetic domains, ?), so they are particles with limited ability to record the geomagnetic field. In addition to the magnetic domain state, particles can still vary in composition, size and shape which causes changes in their magnetic properties. All these factors are crucial in determining stable remanence directions used in the calculation of paleomagnetic poles.

Classic techniques for obtaining paleomagnetic data, e.g., thermal demagnetization and alternating fields, are based on the progressive acquisition of the magnetization contained in cylindrical samples, usually of 10 cm³. The magnetic signal of a single specimen is the result of the sum of moments contained in the assembly of ferromagnetic grains, including stable and unstable registers (?). although there are recent well-structured studies of imaging magnetic minerals in thin-sections (e.g., ?????????), obtaining NRM directions of individual grains in the rock fabric remains, to the best of our knowledge, a challenge deeply explored only by ?. With the possibility of isolating the individual contributions of a fairly large number ($10^6 > N > 10^7$) of stable magnetic particles (SD/PSD) the magnetic directions re-

covered, using the average of their NRM vectors, would have an accurate paleomagnetic response (?), however such number of observations is unfeasible for the currently insufficient measurements scales of the equipments (?).

Several branches of Earth Sciences have demonstrated the importance of the “spatiality” of data on a microscopic scale, mainly in Geochemistry and Geochronology, where it is possible to perform punctual analyzes and compositional maps, which allowed significant advances in the understanding of igneous, metamorphic and sedimentary processes (e.g., ???). In Paleomagnetism there has been an interest in point magnetic analyses, or microscale magnetic maps, from magnetic microscopy techniques (????). However, despite recent advances in this area, still there is no well-established inversion protocol to determine the magnetic vector direction of each individual ferromagnetic grains, nor the intensity of magnetization, without using additional information of the positioning and shape of these sources, such as micromagnetic tomography (e.g., ???), which is a measurement spatially even more limited than the magnetic microscopy itself.

This paper aims to give a new perspective in the methodological routine that carry out paleomagnetic studies in microscale allowing to retrieve the individual remanent magnetization direction of these stable magnetic carriers (SD and PSD), semi automatically and without any additional information. In this way, a larger area of the thin section can be scanned with the objective of increasing the number of observations and, therefore, increasing the reliability of the directional data obtained. We also intend to generate a micromagnetic analysis protocol in an open source software, based on the techniques that will be described below.

2 Methodology

2.1 Scanning Magnetic Microscopy

Scanning magnetic microscopy (SMM) is the imaging technique in which a thin-section sample of geological material is horizontally displaced under a high-precision (fixed) micromagnetometer to obtain magnetization (?). The SMM performed at a fixed height above the sample also has the advantage of facilitating the subtraction of the ambient field (constant), to which it might be subject during the scan (?). The availability of high-performance and low-cost magnetic sensors has promoted a great advance in the application of SMM in recent years. However, its sensitivity is still a few orders of magnitude lower than that of superconducting quantum interference devices (SQUIDS), the latter being between 10^{-12} and 10^{-15} Am² (?). This disadvantage is offset by (i) the high spatial resolution of the SMM, as it is performed at a few tens of micrometers from the sampled surface; and (ii) SQUID magnetic microscopy is performed at low temperatures (< 100K), which can cause changes in the original NRM of the sample, while SMM is performed at room temperature (??).

The SMM can also be considered as a form of aeromagnetic survey, carried out at microscales on sources of flat topography, with high spatial resolution and greater sensitivity to magnetic moment (?). An emerging magnetic imaging technology is the quantum diamond microscope (QDM) with very high spatial resolution ($\cong 1 \mu\text{m}$), and can recover magnetic moments as weak as 10^{-17} Am², through magnetic sensors located at altitudes between 1 and 5 μm relative to the sample surface (?) capable of detecting the magnetic signals of SD magnetite particles (Figure 1). Another promising type of magnetic microscope is the magnetic tunnel junction (MTJ) with a spatial resolution greater than 7 μm , a

magnetic moment sensitivity of up to 10^{-14} Am² and sample-sensor distance of 7 μm . Its advantages reside in the fact that these MTJ devices do not require high bias current to operate (few tens of μA), which avoids induced magnetization signals created by artificial magnetic field during the measurements (?).

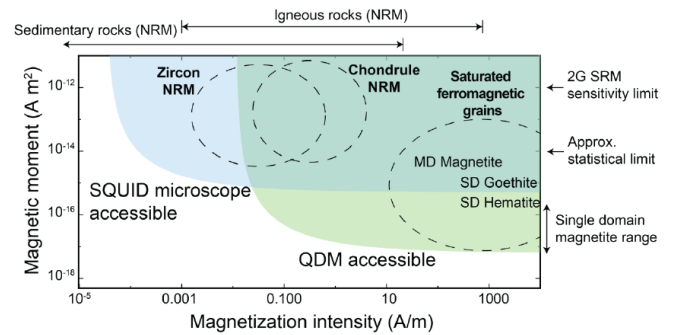


Figure 1: Sample classes accessible to QDM, SQUID microscope and 2G Enterprises SRM. The accessible region for the QDM was calculated assuming a magnetic field noise threshold of 5 nT and a minimum sensor-sample distance of 5 μm . The calculation for the SQUID microscope assumed field noise values of 15 pT and sensor-sample distance of 150 μm . Source: ?.

Due to the similarities between magnetic microscopy techniques and aeromagnetic surveys, the methodologies of data inversion of the latter, densely studied in the last decades, can be adapted for magnetic microscopy. However, ? report important distinctions between SMM and aeromagnetic surveys, namely: (i) the source distribution in the SMM can often be accurately modeled in a two-dimensional model; (ii) the SMM measures the field produced directly by the sample's NRM; (iii) the sensor positioning is very accurate in the SMM, and the vertical component of the magnetic field is usually measured, rather than the total field; (iv) there is no need for correction to bring all measurements to the same surface or to grid the data; and (v) the distributions of the magnetization sources are finite and known.

2.2 Magnetic Inversion

The rapid inversion of the total field is a method developed by ? being computationally efficient to invert

the magnetic anomalies produced by multiple sources with approximately spherical shapes to estimate their magnetization directions (inclination and declination). This methodology requires the central position of the magnetic sources, which can be obtained with Euler Deconvolution, and the information on their geometry helps to reduce the non-exclusivity of the problem. In this way it is possible to estimate the direction of magnetization from multiple sources. The method does not require that all sources have the same magnetization direction nor the use of regularly spaced data on a horizontal grid, and can still be implemented in linear and non-linear inversion problems.

Currently, the main inversion limitations for these type of data are: (i) in part because the sampling scale during measurement is insufficiently accurate and (ii) because of the non-singularity of the magnetic inversion (?). The basic mathematical structure associated with the inverse problem of aeromagnetic data can be adapted and used in SMM data due to its similarity, despite the non-singularity caused by the infinite number of solutions for the same observed magnetic field (?). Assigning as much information as possible about the analyzed sample and the experimental environment can reduce this ambiguity by recovering the magnetization direction. In particles with unidirectional magnetization, and without magnetization sources outside the sample area, it is possible to guarantee singularity for the inverse problem in SMM (?). Associating the fact that there is a singularity in the response of uniformly magnetized particles and that ferromagnetic particles (*l.s.*) with stable magnetization have such a characteristic, therefore, the inversion method becomes ideal for the purpose of this project.

2.2.1 Direct Model

Let \bar{B} be the observed data vector, whose i -th element \bar{B}_i , $i = 1, 2, \dots, N$, is a total field anomaly, resulting from the NRM contribution of each ferromagnetic particle (*l.s.*), measured at position (x_i, y_i, z_i) (black dots, Figure 2). In this cartesian coordinate system, x points to geographic north, y points east, and z points down. In general, the magnetic field that is produced in the thin section is the result solely and exclusively of the NRM contribution of the particles without considering the induced component, since the measurements carried out in the magnetic microscope are usually made under magnetic shielding conditions. Thereby, approximating the shape of ferromagnetic minerals (*l.s.*) to NRM magnetizing spheric/punctual sources. According to ? the equation of a uniformly magnetized sphere is given by:

$$b = C_m \cdot \frac{4}{3} \cdot \pi \cdot R^3 \cdot m \cdot \hat{n} \cdot \frac{1}{r^2} \cdot \hat{r} \quad (1)$$

Whereas the magnetic sources can be represented by a set of L uniformly magnetized spheres. In this case, each sphere will have a contribution in the field measured at the position (x_i, y_i, z_i) :

$$b_i^j = C_m \cdot \frac{4}{3} \pi \cdot R_j^3 \cdot \bar{m}^j \cdot \frac{1}{r_{i,j}^2} \cdot \hat{r}_{i,j}, \quad j = 1, 2, \dots, L \quad (2)$$

Where: $C_m = \frac{\mu_0}{4\pi} = 10^{-7} \frac{H}{m}$; R_j is the radius of the j -th sphere; (unit vector $\hat{r}_{i,j}$) between the center of the j -th sphere and the observation point; $i = 1, 2, \dots, N$; and $\bar{m}^j = [mx_j \ my_j \ mz_j]^T$ is the vector formed by the components of the magnetization of the j -th sphere (unit vector \hat{m}^j).

Thus, the total magnetization measured at the position (x_i, y_i, z_i) will be the sum of contributions from the L spheres, given by:

$$B_i = \sum_{j=1}^L b_i^j \quad (3)$$

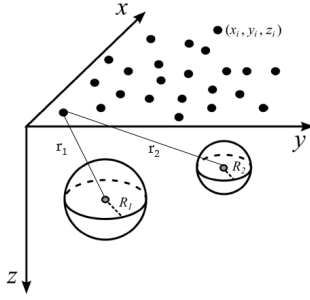


Figure 2: Schematic representation of spheres ($L = 2$) uniformly magnetized in the subsurface, whose magnetic effect, produced by these spheres, can be observed at points (x_i, y_i, z_i) , $i = 1, 2, \dots, N$ (points black). In this cartesian coordinate system, x points to geographic north, y points east, and z points down. Modified from: ?.

According to ? the Equation (2) can be segmented into two members: (i) the first being a matrix M_i^j encompassing the vector relationship with the positioning for each source and (ii) the second being h_j , which is the vector that encompasses the cartesian components of the magnetization of each sphere:

$$M_i^j = \begin{bmatrix} \left(\frac{\partial^2}{\partial x \partial x} \cdot \frac{1}{r_{i,j}} \right) & \left(\frac{\partial^2}{\partial x \partial y} \cdot \frac{1}{r_{i,j}} \right) & \left(\frac{\partial^2}{\partial x \partial z} \cdot \frac{1}{r_{i,j}} \right) \\ \left(\frac{\partial^2}{\partial x \partial y} \cdot \frac{1}{r_{i,j}} \right) & \left(\frac{\partial^2}{\partial y \partial y} \cdot \frac{1}{r_{i,j}} \right) & \left(\frac{\partial^2}{\partial y \partial z} \cdot \frac{1}{r_{i,j}} \right) \\ \left(\frac{\partial^2}{\partial x \partial z} \cdot \frac{1}{r_{i,j}} \right) & \left(\frac{\partial^2}{\partial y \partial z} \cdot \frac{1}{r_{i,j}} \right) & \left(\frac{\partial^2}{\partial z \partial z} \cdot \frac{1}{r_{i,j}} \right) \end{bmatrix}_{3N \times 3L} \quad (4)$$

$$\text{Where: } \frac{1}{r_j} \equiv \frac{1}{\sqrt{(x_i - x_{c_j})^2 + (y_i - y_{c_j})^2 + (z_i - z_{c_j})^2}}$$

Subsequently, the components of the total magnetizing field can be obtained (from Equation (3)), as shown below:

$$\begin{bmatrix} \left(\frac{\partial^2}{\partial x \partial x} \cdot \frac{1}{r_{i,j}} \right) & \left(\frac{\partial^2}{\partial x \partial y} \cdot \frac{1}{r_{i,j}} \right) & \left(\frac{\partial^2}{\partial x \partial z} \cdot \frac{1}{r_{i,j}} \right) \\ \left(\frac{\partial^2}{\partial x \partial y} \cdot \frac{1}{r_{i,j}} \right) & \left(\frac{\partial^2}{\partial y \partial y} \cdot \frac{1}{r_{i,j}} \right) & \left(\frac{\partial^2}{\partial y \partial z} \cdot \frac{1}{r_{i,j}} \right) \\ \left(\frac{\partial^2}{\partial x \partial z} \cdot \frac{1}{r_{i,j}} \right) & \left(\frac{\partial^2}{\partial y \partial z} \cdot \frac{1}{r_{i,j}} \right) & \left(\frac{\partial^2}{\partial z \partial z} \cdot \frac{1}{r_{i,j}} \right) \end{bmatrix}_{3N \times 3L}$$

As in the specific case in the study of magnetic microscopy, in the routine practice, the vertical component of magnetization is usually measured. In this case, there is a need to adapt the Equation (5) to isolate the response from the vertical component (B_z). Therefore, the equation of the direct model will be given by:

$$\begin{bmatrix} \left(\frac{\partial^2}{\partial x \partial x} \cdot \frac{1}{r_{i,j}} \right) & \left(\frac{\partial^2}{\partial y \partial y} \cdot \frac{1}{r_{i,j}} \right) & \left(\frac{\partial^2}{\partial z \partial z} \cdot \frac{1}{r_{i,j}} \right) \end{bmatrix}_{N \times 3L} \cdot \begin{bmatrix} mx_j \cdot C_m \cdot \frac{4}{3} \pi \cdot R_j^3 \\ my_j \cdot C_m \cdot \frac{4}{3} \pi \cdot R_j^3 \\ mz_j \cdot C_m \cdot \frac{4}{3} \pi \cdot R_j^3 \end{bmatrix}_{3L \times 1} \quad (6)$$

The magnetization is usually represented in spherical coordinates of intensity (Q (A/m)), declination (D (°)) and inclination (I (°)). Thus, the vector \bar{m}_j , containing the cartesian coordinates of magnetization, of the direct model can also be calculated as follows:

$$\begin{bmatrix} mx_j \\ my_j \\ mz_j \end{bmatrix}_{3L \times 1} = Q_j \cdot \begin{bmatrix} \cos(I_j) \cdot \cos(D_j) \\ \cos(I_j) \cdot \sin(D_j) \\ \sin(I_j) \end{bmatrix}_{3L \times 1} \quad (7)$$

We can simplify the Equation (6) to:

$$\begin{bmatrix} \left(\frac{\partial^2}{\partial x \partial x} \cdot \frac{1}{r_{i,j}} \right) & \left(\frac{\partial^2}{\partial y \partial y} \cdot \frac{1}{r_{i,j}} \right) & \left(\frac{\partial^2}{\partial z \partial z} \cdot \frac{1}{r_{i,j}} \right) \end{bmatrix}_{N \times 3L} \cdot \begin{bmatrix} hx_j \\ hy_j \\ hz_j \end{bmatrix}_{3L \times 1} = [Bz_i] \quad (8)$$

With this, the Equation (8) can be rewritten in linear form, given by:

$$\bar{M} \cdot \bar{h}_j = \bar{B}_z \quad (9)$$

2.2.2 Inverse Model

Assuming that the ferromagnetic minerals (*l.s.*) that

give rise to the observed magnetization component data vector \bar{B}_z can be approximated by a set of L uniformly magnetized spheres with known coordinates $(x_{c_j}, y_{c_j}, z_{c_j})$, $j = 1, 2, \dots, L$, of their centers. Also assuming that

there is no induced magnetization component, only that of the NRM. Under these assumptions, a superdetermined inverse linear problem is formulated to estimate the vector of parameters \bar{h} (Equation (9)) from the observed data \bar{B}_z and \bar{M} , the latter being obtained previously with the Euler Deconvolution.

The problem of estimating a parameter vector \bar{h} containing the spheres' magnetization vectors can be solved by minimizing the objective function $f(\bar{h})$:

$$f(\bar{h}) = \|e\|^2 = e^T \cdot e = (\bar{M}^T \cdot \bar{h} - \bar{d})^T \cdot (\bar{M}^T \cdot \bar{h} - \bar{B}_z) \quad (10)$$

When differentiating the (Equation (10)) by \bar{h} and equating the result to the zero vector ($\frac{\partial f}{\partial \bar{h}_k} = \bar{0}$). Then we obtain the normal equation for estimating least squares solution given by:

$$\bar{h} = (\bar{M}^T \cdot \bar{M})^{-1} \cdot (\bar{M}^T \cdot \bar{B}_z) \quad (11)$$

As the least squares estimate (Equation (11)) is very sensitive to the presence of outliers in the observed data, the estimated parameters could be seriously misleading. To counteract this problem ? suggest a robust scheme based on the minimization of the objective function obtained with the absolute error:

$$f(\tilde{h}) = \left(\sum_{i=1}^N \left| (\bar{M}^T \cdot \tilde{h})_i - (\bar{B}_z)_i \right| \right) \quad (12)$$

Unlike the solution presented for the objective function in Equation (11), the parameter vector minimizing Equation (12) cannot be obtained as a simple linear system. A practical way is the iteratively reweighted least squares algorithm (??). In this algorithm, at each iteration k , the following linear system is solved:

$$\tilde{h}^{k+1} = (\bar{M}^T \cdot \bar{R}^k \cdot \bar{M})^{-1} \cdot (\bar{M}^T \cdot \bar{R}^k \cdot \bar{B}_z) \quad (13)$$

The term \bar{R}^k is an $N \times N$ diagonal matrix whose i -th element r_i^k ($i = 1, 2, \dots, N$) is given by:

$$r_i^k = \frac{1}{\left| (\bar{M}^T \cdot \tilde{h})_i - \bar{B}_{zi} + e \right|} \quad (14)$$

Where: e is a small positive number used to prevent singularities

This iterative process starts ($k = 0$) with the solution vector obtained by the least squares estimator (Equa-

tion (11)). From this initial approximation \tilde{h}^0 , we calculate the matrix \bar{R}^0 (Equation (14)). Which is used in the solution of the linear system given by Equation (13) to obtain the estimate \tilde{h}^1 . Later using this updated estimate to calculate the new matrix \bar{R}^1 (Equation (14)), we solve the linear system (Equation (13)) to obtain a new estimate \tilde{h}^2 , and so on. As the iterations progress, this iterative procedure tends to converge and estimate \tilde{h} , which is called robust estimate (?). According to ? this convergence can be limited by a tolerance τ , given by:

$$\frac{\|\tilde{h}^{k+1} - \tilde{h}^k\|}{1 + \|\tilde{h}^{k+1}\|} \leq \tau \quad (15)$$

Where: τ is a positive number (*e.g.*, 10^{-2}) chosen by the algorithm user.

2.2.3 Directions of Magnetization and Uncertainty Propagation

In paleomagnetic studies the magnetization vectors are represented in terms of their declination (D) and inclination (I). These are given as a function of the magnetization vector \bar{h}_j (Equation (8)) and represented in spherical coordinates (as shown in Figure 3).

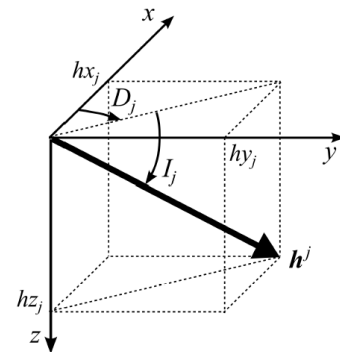


Figure 3: Schematic representation of vector h_j (Equation (8)) with elements hx_j , hy_j and hz_j in cartesian coordinates. This vector has declination D_j (positive clockwise) and slope I_j (positive downwards), $j = 1, 2, \dots, L$. Source: ?.

In this way, it is possible to determine the magnetization directions D_j and I_j for the j -th sphere of the set of

L spheres by using:

$$D_j = \tan^{-1} \left(\frac{hy_j}{hx_j} \right) \quad (16)$$

$$I_j = \tan^{-1} \left(\frac{hz_j}{\sqrt{(hx_j)^2 + (hy_j)^2}} \right) \quad (17)$$

In a micromagnetic survey, or any geophysical survey, measurements are affected by noise caused by experimental errors and equipment inaccuracies. Noise in the observed data vector \bar{B}_z affects the solution of the estimated parameter vector \bar{h}_j , regardless of the method used. Assuming that the noise during the measurement of the observed data is independent and with variance σ_0^2 , one can quantify this effect on the estimated parameters through propagation of the covariance (?).

The covariance matrix of these parameters will be given by:

$$Cov(\bar{h}_j) = \sigma_0^2 \cdot (\bar{M}^T \cdot \bar{M})^{-1} \quad (least\ square) \quad (18)$$

$$Cov(\tilde{h}_j) = \sigma_0^2 \cdot (\bar{M}^T \cdot \bar{R}^k \cdot \bar{M})^{-1} \quad (robust) \quad (19)$$

The main diagonal of the covariance matrix (Equation (18) and Equation (19)) contains the variance of each member of the parameter vector, as expressed below:

$$Cov = \begin{bmatrix} Var(hx_1) & \dots & \dots & \dots & \dots & \dots & \dots \\ \dots & Var(hy_1) & \dots & \dots & \dots & \dots & \dots \\ \dots & \dots & Var(hz_1) & \dots & \dots & \dots & \dots \\ \dots & \dots & \dots & \ddots & \dots & \dots & \dots \\ \dots & \dots & \dots & \dots & Var(hx_L) & \dots & \dots \\ \dots & \dots & \dots & \dots & \dots & Var(hy_L) & \dots \\ \dots & \dots & \dots & \dots & \dots & \dots & Var(hz_L) \end{bmatrix} \quad (20)$$

Thus, for the j-th sphere:

$$\sigma_{hx_j} = \sqrt{Var(hx_j)}, \quad \sigma_{hy_j} = \sqrt{Var(hy_j)} \quad \text{and} \quad \sigma_{hz_j} = \sqrt{Var(hz_j)} \quad (21)$$

Thus, the propagation of uncertainties of the declination (D_j) and slope (I_j) results are given as a function of the parameters obtained in Equation (21):

$$\sigma_{D_j} = \sqrt{\left(\frac{\partial D_j}{\partial hx_j} \right)^2 \cdot (\sigma_{hx_j})^2 + \left(\frac{\partial D_j}{\partial hy_j} \right)^2 \cdot (\sigma_{hy_j})^2} \quad (22)$$

$$\sigma_{I_j} = \sqrt{\left(\frac{\partial I_j}{\partial hx_j} \right)^2 \cdot (\sigma_{hx_j})^2 + \left(\frac{\partial I_j}{\partial hy_j} \right)^2 \cdot (\sigma_{hy_j})^2 + \left(\frac{\partial I_j}{\partial hz_j} \right)^2 \cdot (\sigma_{hz_j})^2} \quad (23)$$

Where:

$$\frac{\partial D_j}{\partial hx_j} = \frac{-hy_j}{hx_j^2 + hy_j^2} \quad (24)$$

$$\frac{\partial D_j}{\partial hy_j} = \frac{hx_j}{hx_j^2 + hy_j^2} \quad (25)$$

$$\frac{\partial I_j}{\partial hx_j} = \frac{-hx_j \cdot hz_j}{\sqrt{hx_j^2 + hy_j^2} \cdot (hx_j^2 + hy_j^2 + hz_j^2)} \quad (26)$$

$$\frac{\partial I_j}{\partial hy_j} = \frac{-hy_j \cdot hz_j}{\sqrt{hx_j^2 + hy_j^2} \cdot (hx_j^2 + hy_j^2 + hz_j^2)} \quad (27)$$

$$\frac{\partial I_j}{\partial hz_j} = \frac{\sqrt{hx_j^2 + hy_j^2}}{(hx_j^2 + hy_j^2 + hz_j^2)} \quad (28)$$

2.3 Euler Deconvolution

Euler Deconvolution is a consolidated method classically applied to data from aeromagnetic surveys. Given the similarities between SMM and aeromagnetic data, its application becomes plausible for determining the positions of magnetic sources caused by ferromagnetic minerals (l.s). Euler deconvolution is one of the most useful methods for estimating the three-dimensional positioning of magnetic sources/geological bodies (??). It is the

application of a mobile operator in a small data window over the sampled data set. The observations made within this window are used to estimate the horizontal and vertical positions of the source by solving a small linear system of equations using the gradients of the potential field, provided that the shapes of the sources are assumed.

Despite this, this system usually has a large number of solutions (?), which becomes a limitation for the method. In an attempt to circumvent the problem of this expressive cloud of solutions, we suggest the previous application of a method of delimitation of the contours of the sources generating the potential field and later the application of Euler's Deconvolution, which becomes unique for each source (one data window per source). As the method itself already requires the gradients of the potential field, therefore, the method of delimitation chosen was the horizontal gradient (?). ? states that the response of a source's horizontal gradient tends to overlap its limits, thus obtaining a two-dimensional robust map of the sources location. The amplitude of the horizontal gradient (∇H) is expressed by Equation (29). Once the source positions are determined by this preliminary method then, subsequently, Euler Deconvolution is applied and a static window for each source generating the potential field.

$$\nabla H = \sqrt{\left(\frac{\partial F}{\partial x}\right)^2 + \left(\frac{\partial F}{\partial y}\right)^2} \quad (29)$$

2.3.1 Euler Deconvolution Formulation

The anomaly of a potential field F produced by a three-dimensional source, whose cartesian coordinates of its central position are x_0 , y_0 and z_0 , satisfies the homogeneous Euler equation (?) expressed by:

$$(x-x_0) \cdot \frac{\partial F}{\partial x} + (y-y_0) \cdot \frac{\partial F}{\partial y} + (z-z_0) \cdot \frac{\partial F}{\partial z} = n \cdot (b-F) \quad (30)$$

where: n is the structural index, that is, a gauge of the geometric sources causing the anomaly; and b is the constant, and unknown.

The Euler's Deconvolution uses the gradient of a potential field and the structural index, which can be defined by the geometric nature of the sources. The structural index is the only necessary a priori knowledge. Once a value for n is assumed ($n = 3$ for spherical/punctual magnetic sources), the homogeneous Euler equation can be rearranged as follows:

$$x_0 \cdot \frac{\partial F}{\partial x} + y_0 \cdot \frac{\partial F}{\partial y} + z_0 \cdot \frac{\partial F}{\partial z} + n \cdot b = x \cdot \frac{\partial F}{\partial x} + y \cdot \frac{\partial F}{\partial y} + z \cdot \frac{\partial F}{\partial z} + n \cdot F \quad (31)$$

The Equation (31) can be written in matrix form as:

$$\begin{bmatrix} Fx_1 & Fy_1 & Fz_1 & n \\ Fx_2 & Fy_2 & Fz_2 & n \\ \vdots & \vdots & \vdots & \vdots \\ Fx_N & Fy_N & Fz_N & n \end{bmatrix} \begin{bmatrix} x_0 \\ y_0 \\ z_0 \\ b \end{bmatrix} = \begin{bmatrix} x_1 \cdot Fx_1 + y_1 \cdot Fy_1 + z_1 \cdot Fz_1 \\ x_2 \cdot Fx_2 + y_2 \cdot Fy_2 + z_2 \cdot Fz_2 \\ \vdots \\ x_N \cdot Fx_N + y_N \cdot Fy_N + z_N \cdot Fz_N \end{bmatrix} \quad (32)$$

Where: Fx_i , Fy_i and Fz_i represent, respectively, the gradients $\frac{\partial F}{\partial x}$, $\frac{\partial F}{\partial y}$ and $\frac{\partial F}{\partial z}$ evaluated on the i -th observation point ($i = 1, 2, \dots, N$). While x_i , y_i and z_i represent the cartesian coordinates at the i -th observation point.

Note that Equation (32) is a linear system $\bar{G} \cdot \bar{m} = \bar{d}$ and its objective function $f(\bar{m})$ expressed by:

$$f(\bar{m}) = \|e\|^2 = (\bar{G} \cdot \bar{m} - \bar{d})^T \cdot (\bar{G} \cdot \bar{m} - \bar{d}) \quad (33)$$

The solution \bar{m} of the system can be obtained by minimizing the objective function ($\frac{\partial f}{\partial m_k} = 0$) through the least squares estimator given by:

$$\bar{m} = \left(\bar{G}^T \cdot \bar{G} \right)^{-1} \cdot \left(\bar{G}^T \cdot \bar{d} \right) \quad (34)$$

Thus, $\bar{m} = [x_0 \ y_0 \ z_0 \ b]^T$ will be the solution vector that satisfies Euler's Equation with the least possible error containing the position coordinates font center (x_0 , y_0 , z_0) and the base level (b).

3 Results

3.1 Synthetic Data

We applied the proposed method in a numerical simulation of a geological thin-section of dimensions 1000 μm x 1000 μm in a regular grid (1000 x 1000) for estimating the magnetization directions of four spherical sources uniformly magnetized (but different directions), according to Table 1. Totaling an observation number $N = 10^6$ obtained at a sensor-sample distance of 5 μm and a spacing of 1 μm . Subsequently, a pseudorandom noise of normal Gaussian distribution, with a zero mean and standard variation $\cong 5\%$ of the anomaly amplitude, was added to the data as shown in Figure XX.

Table 1: Initial position and magnetization parameters for each spherical source.

Sphere	Center coordinates			Magnetization		
	X (μm)	Y (μm)	Z (μm)	Q (A/m)	D (°)	I (°)
1	250	250	8.50	6.0	-140	-30
2	500	500	10.0	6.0	0	62
3	750	750	5.30	6.0	-70	-50
4	200	800	7.75	6.0	125	22

3.1.1 Euler Solution

The first step is to calculate the magnetic horizontal gradient in order to isolate the window data of each source. In the horizontal gradient, the magnetic anomaly caused by a body tends to overlap its limits, thus obtaining a robust positioning (?). ?.

Table 2: Central positions of sources input vs Euler deconvolution solutions.

Esfera	Posição do Centro de Entrada			Solução de Euler	
	X (μm)	Y (μm)	Z (μm)	X (μm)	Y (μm)
1	250	250	8.50	249.144984	250.08469
2	500	500	10.0	500.213134	500.44363
3	750	750	5.30	749.873747	750.12783
4	200	800	7.75	200.177971	800.33101

Table 3: Input magnetization directions vs inversion solutions and their error propagation.

Esfera	Direção de Entrada		Direções Recuperadas e Incertezas		
	D (°)	I (°)	D (°)	σ D (°)	I (°)
1	-140	-30	-137.0294	± 0.7641	-32.6550
2	0	62	2.5167	± 1.5004	60.5473
3	-70	-50	-68.3316	± 0.6752	-49.0172
4	125	22	124.8320	± 0.6449	21.9940

4 Discussion

5 Conclusion

6 Data and code availability

The Python source code used to produce all results and figures presented here is available at <https://doi.org/10.6084/m9.figshare.13604360> and <https://github.com/compgeolab/eql-gradient-boosted> under the BSD 3-clause open-source license.

The gradient-boosted equivalent sources implementation is based on the equivalent source code in the Harmonica library (Uieda et al., 2020b). Other software used in this study includes: Pooch (Uieda et al., 2020a) for downloading and caching datasets, Verde (Uieda, 2018) for block reductions and coordinate manipulations, Boule (Uieda and Soler, 2020) for normal gravity calculations, xarray (Hoyer and Hamman, 2017) and Numpy (Harris et al., 2020) for handling multidimensional arrays and numerical computations, Numba (Lam et al., 2015) for just-in-time compilation and parallelization, scikit-learn (Pedregosa et al., 2011) for cross-validation, Matplotlib (Hunter, 2007) and PyGMT (Uieda et al., 2020c) for generating the figures and maps, and the Jupyter note-

book programming environment (Kluyver et al., 2016).

Harmonica, Boule, Pooch, and Verde are part of the Fatiando a Terra project (Uieda et al., 2013).

All datasets used are open-access and publicly available. The synthetic surveys were generated using a public domain gravity dataset for Southern Africa distributed by the NOAA NCEI (<https://www.ngdc.noaa.gov/mgg/gravity/gravity.html>) and the Great Britain Aeromagnetic Survey distributed by the British Geological Survey (BGS) under an Open Government License (<https://www.bgs.ac.uk/products/geophysics/aeromagneticRegional.html>). The shaded relief in Fig. ?? is the SRTM15+ dataset by Tozer et al. (2019). The Australian ground gravity data is based on a compilation distributed by Geoscience Australia under a Creative Commons Attribution 4.0 International Licence (Wynne, 2018) which was filtered and referenced to the WGS84 ellipsoid by Uieda (2021) and is distributed under the same license (<https://doi.org/10.6084/m9.figshare.13643837>).

7 Acknowledgements

We are indebted to the developers and maintainers of the open-source software without which this work would not have been possible. We would also like to thank Editor Frederik Simons, Assistant Editor Fern Storey, and two anonymous reviewers for their constructive comments. S.R. Soler is supported by a scholarship from CONICET, Argentina. This work contains British Geological Survey materials © UKRI. S.R. Soler and L. Uieda jointly developed the initial idea, analysed the results, and wrote the paper. S.R. Soler produced all results and developed the software implementation with the assistance of L. Uieda.

References

- Harris, C. R., Millman, K. J., van der Walt, S. J., Gommers, R., Virtanen, P., Cournapeau, D., Wieser, E., Taylor, J., Berg, S., Smith, N. J., Kern, R., Picus, M., Hoyer, S., van Kerkwijk, M. H., Brett, M., Haldane, A., del Río, J. F., Wiebe, M., Peterson, P., G'erard-Marchant, P., Sheppard, K., Reddy, T., Weckesser, W., Abbasi, H., Gohlke, C., and Oliphant, T. E. (2020). Array programming with NumPy. *Nature*, 585(7825):357–362. doi:[10.1038/s41586-020-2649-2](https://doi.org/10.1038/s41586-020-2649-2).
- Hoyer, S. and Hamman, J. (2017). xarray: N-D labeled arrays and datasets in Python. *Journal of Open Research Software*, 5(1). doi:[10.5334/jors.148](https://doi.org/10.5334/jors.148).
- Hunter, J. D. (2007). Matplotlib: A 2D graphics environment. *Computing in Science & Engineering*, 9(3):90–95. doi:[10.1109/MCSE.2007.55](https://doi.org/10.1109/MCSE.2007.55).
- Kluyver, T., Ragan-Kelley, B., Pérez, F., Granger, B., Bussonnier, M., Frederic, J., Kelley, K., Hamrick, J., Grout, J., Corlay, S., Ivanov, P., Avila, D., Abdalla, S., and Willing, C. (2016). Jupyter Notebooks – a publishing format for reproducible computational workflows. In Loizides, F. and Schmidt, B., editors, *Positioning and Power in Academic Publishing: Players, Agents and Agendas*, pages 87 – 90. IOS Press.
- Lam, S. K., Pitrou, A., and Seibert, S. (2015). Numba. In *Proceedings of the Second Workshop on the LLVM Compiler Infrastructure in HPC - LLVM '15*. ACM Press. doi:[10.1145/2833157.2833162](https://doi.org/10.1145/2833157.2833162).
- Pedregosa, F., Varoquaux, G., Gramfort, A., Michel, V., Thirion, B., Grisel, O., Blondel, M., Prettenhofer, P., Weiss, R., Dubourg, V., Vanderplas, J., Passos, A., Cournapeau, D., Brucher, M., Perrot, M., and Duchesnay, E. (2011). Scikit-learn: Machine learning in Python. *Journal of Machine Learning Research*, 12:2825–2830.
- Tozer, B., Sandwell, D. T., Smith, W. H. F., Olson,

- C., Beale, J. R., and Wessel, P. (2019). Global Bathymetry and Topography at 15 Arc Sec: SRTM15+. *Earth and Space Science*, 6(10):1847–1864. doi:[10.1029/2019ea000658](https://doi.org/10.1029/2019ea000658).
- Uieda, L. (2018). Verde: Processing and gridding spatial data using Green’s functions. *Journal of Open Source Software*, 3(29):957. doi:[10.21105/joss.00957](https://doi.org/10.21105/joss.00957).
- Uieda, L. (2021). Ground gravity data compilation for Australia filtered by survey quality and packaged in CF-compliant netCDF. doi:[10.6084/M9.FIGSHARE.13643837](https://doi.org/10.6084/M9.FIGSHARE.13643837).
- Uieda, L., Jr, V. C. O., and Barbosa, V. C. F. (2013). Modeling the Earth with Fatiando a Terra. In van der Walt, S., Millman, J., and Huff, K., editors, *Proceedings of the 12th Python in Science Conference*, pages 96 – 103. doi:[10.25080/Majora-8b375195-010](https://doi.org/10.25080/Majora-8b375195-010).
- Uieda, L., Soler, S., Rampin, R., van Kemenade, H., Turk, M., Shapero, D., Banihirwe, A., and Leeman, J. (2020a). Pooch: A friend to fetch your data files. *Journal of Open Source Software*, 5(45):1943. doi:[10.21105/joss.01943](https://doi.org/10.21105/joss.01943).
- Uieda, L. and Soler, S. R. (2020). Boule v0.2.0: Reference ellipsoids for geodesy, geophysics, and coordinate calculations. doi:[10.5281/zenodo.3939204](https://doi.org/10.5281/zenodo.3939204).
- Uieda, L., Soler, S. R., Pesce, A., Oliveira Jr, V. C., and Shea, N. (2020b). Harmonica: Forward modeling, inversion, and processing gravity and magnetic data. doi:[10.5281/zenodo.3628742](https://doi.org/10.5281/zenodo.3628742).
- Uieda, L., Tian, D., Leong, W. J., Toney, L., Newton, T., and Wessel, P. (2020c). PyGMT: A Python interface for the Generic Mapping Tools. doi:[10.5281/zenodo.4253459](https://doi.org/10.5281/zenodo.4253459).
- Wynne, P. (2018). NetCDF Ground Gravity Point Surveys Collection. doi:[10.26186/5C1987FA17078](https://doi.org/10.26186/5C1987FA17078).

A Source position parameters used for the tests on synthetic data

Tables 4 and 5 show the parameter values tested and their optimal values for creating the equivalent source distributions tested in Section ???. The optimal values were used to produce the results in Figs ?? and ??.

Table 4: Parameters used to produce each source distribution for interpolating the synthetic ground survey data. Also contains the set of parameters that generates the smallest RMS error for each source distribution and their corresponding RMS.

Source layout	Depth type	Parameters	Values	Best	RMS
Source Below Data	Constant	Depth (m)	1000 to 17000, step size 2000	7000	0.78
		Damping	10^{-4} , 10^{-3} , ..., 10^2	10^{-1}	
	Relative	Depth (m)	1000 to 17000, step size 2000	9000	0.79
		Damping	10^{-4} , 10^{-3} , ..., 10^2	10^{-1}	
	Variable	Depth (m)	0 to 1400, step size 200	1000	0.80
		Depth factor	0.1, 0.5, 1, 2, 3, 4, 5 and 6	1	
		k neighbours	1, 5, 10 and 15	15	
		Damping	10^{-4} , 10^{-3} , ..., 10^2	1	
Block Averaged Sources	Constant	Depth (m)	1000 to 17000, step size 2000	7000	0.77
		Block size (m)	1000, 2000, 3000 and 4000	3000	
		Damping	10^{-4} , 10^{-3} , ..., 10^2	10^{-1}	
	Relative	Depth (m)	1000 to 17000, step size 2000	7000	0.79
		Block size (m)	1000, 2000, 3000 and 4000	3000	
		Damping	10^{-4} , 10^{-3} , ..., 10^2	10^{-1}	
	Variable	Depth (m)	0 to 1400, step size 200	600	0.72
		Depth factor	0.1, 0.5, 1, 2, 3, 4, 5 and 6	1	
		k neighbours	1, 5, 10 and 15	15	
		Block size (m)	1000, 2000, 3000 and 4000	3000	
		Damping	10^{-4} , 10^{-3} , ..., 10^2	10^{-1}	
Grid Sources	Constant	Depth (m)	1000 to 9000, step size 2000	3000	0.97
		Grid spacing (m)	1000, 2000, 3000 and 4000	2000	
		Damping	10^1 , 10^2 , 10^3 and 10^4	10^2	

Table 5: Parameters used to produce each source distribution for interpolating the synthetic airborne survey data. Also contains the set of parameters that generates the smallest RMS error for each source distribution and their corresponding RMS.

Source layout	Depth type	Parameters	Values	Best	RMS
Source Below Data	Constant	Depth (m)	1000 to 17000, step size 2000	7000	0.35
		Damping	10^{-4} , 10^{-3} , ..., 10^2	10^{-2}	
	Relative	Depth (m)	1000 to 17000, step size 2000	9000	0.35
		Damping	10^{-4} , 10^{-3} , ..., 10^2	10^{-2}	
	Variable	Depth (m)	50 to 1450, step size 200	1450	0.36
		Depth factor	1 to 6, step size 1	1	
		k neighbours	1, 5, 10 and 15	15	
		Damping	10^{-4} , 10^{-3} , ..., 10^2	1	
Block Averaged Sources	Constant	Depth (m)	1000 to 17000, step size 2000	9000	0.34
		Block size (m)	1000, 2000, 3000 and 4000	3000	
		Damping	10^{-4} , 10^{-3} , ..., 10^2	10^{-4}	
	Relative	Depth (m)	1000 to 17000, step size 2000	9000	0.34
		Block size (m)	1000, 2000, 3000 and 4000	2000	
		Damping	10^{-4} , 10^{-3} , ..., 10^2	10^{-3}	
	Variable	Depth (m)	50 to 1450, step size 200	50	0.33
		Depth factor	1 to 6, step size 1	2	
		k neighbours	1, 5, 10 and 15	15	
		Block size (m)	1000, 2000, 3000 and 4000	2000	
		Damping	10^{-4} , 10^{-3} , ..., 10^2	10^{-2}	
Grid Sources	Constant	Depth (m)	1000 to 9000, step size 2000	7000	0.34
		Grid spacing (m)	1000, 2000 and 3000	1000	
		Damping	10^{-3} , 10^{-2} , ..., 10^2	10^{-1}	